analytica

MDPI

Article

Multimodal Imaging of Metals in a Retinal Degeneration Model to Inform on Ocular Disease

Joshua Millar [1], Luke Gibbons [2], Catia Costa [3], Ella Schneider [3], Johanna von Gerichten [4], Melanie J. Bailey [4], Susan Campbell [1], Catherine Duckett [1], Sarah Doyle [2] and Laura M. Cole [1,*]

[1] Centre for Mass Spectrometry Imaging, Biomolecular Sciences Research Centre, Sheffield Hallam University, Sheffield S1 1WB, UK; j.millar@shu.ac.uk (J.M.); hwbsc1@shu.ac.uk (S.C.); catherine_sanders@hotmail.co.uk (C.D.)

[2] Immunobiology Research Group, Department of Clinical Medicine, Trinity College Institute of Neuroscience (TCIN), School of Medicine, Trinity College Dublin (TCD), D02 R590 Dublin, Ireland; lgibbon@tcd.ie (L.G.); doyles8@tcd.ie (S.D.)

[3] Ion Beam Centre, University of Surrey, Guildford GU2 7XH, UK; c.d.costa@surrey.ac.uk (C.C.); e.b.schneider@surrey.ac.uk (E.S.)

[4] Department of Chemistry, University of Surrey, Guildford GU2 7XH, UK; j.vongerichten@surrey.ac.uk (J.v.G.); m.bailey@surrey.ac.uk (M.J.B.)

* Correspondence: l.cole@shu.ac.uk

Abstract: The metallome has been involved in the pathological investigation into ocular tissue for decades; however, as technologies advance, more information can be ascertained from individual tissue sections that were not previously possible. Herein, a demonstration of complementary techniques has been utilized to describe the distribution and concentrations of essential metals in both wildtype (WT) and rhodopsin ($Rho^{-/-}$) ocular tissues. The multimodal approach described is an example of complementary datasets that can be produced when employing a multifaceted analytical approach. Heterogenous distributions of copper and zinc were observable within both WT and $Rho^{-/-}$ tissue by laser ablation inductively coupled plasma mass spectrometry (LA-ICP-MS), and the distributions of further trace elements notoriously problematic for ICP-MS analysis (phosphorous, Sulfur, chlorine, potassium, calcium, iron, and aluminum) were analysed by particle-induced X-ray emission (PIXE).

Keywords: multimodal; laser ablation; ICP-MS; PIXE; IBA; ocular tissue; quantitative; metallomics; age-related macular degeneration

Citation: Millar, J.; Gibbons, L.; Costa, C.; Schneider, E.; von Gerichten, J.; Bailey, M.J.; Campbell, S.; Duckett, C.; Doyle, S.; Cole, L.M. Multimodal Imaging of Metals in a Retinal Degeneration Model to Inform on Ocular Disease. *Analytica* **2023**, *4*, 264–279. https://doi.org/10.3390/analytica4030021

Academic Editor: Marcello Locatelli

Received: 31 May 2023
Revised: 23 June 2023
Accepted: 24 June 2023
Published: 1 July 2023

1. Introduction

As our populations begin to age, the global prevalence of blindness is rising, and with it demands for eye health services [1]. Though many causes of visual impairment may be treated, age-related macular degeneration, one of the most prevalent ocular diseases, has a poor prognosis. Patients with age-related macular degeneration, a disease that accounts for 8.7% of blindness worldwide, can only receive treatment if they are within the 15% of age-related macular degeneration (AMD) patients that have 'wet' AMD [2,3]. The remainder, those with dry AMD, have only preventative measures to rely on [4]. Whilst age, genetics, and environmental factors such as workplace exposure or smoking have been linked to the onset of AMD, the pathology is still poorly understood.

The innate immune system has been heavily associated with AMD in recent years, with some reports suggesting a role of the inflammasome and, more broadly, chronic inflammation as a marker or cause of AMD. These findings are closely associated with the cellular senescence that happens alongside physiological dysregulation in aging, resulting in a buildup of extracellular matrix and debris from dead and dying cells, known as damage-associated molecular patterns (DAMPs), which, through activation of pattern recognition receptors (PRRs), activate the innate immune response [5,6]. Evidence of a feedback loop

of this mechanism results in chronic inflammation in the ocular tissue, producing reactive oxygen species (ROS), which must be eliminated.

For as long as two decades, postulations that essential trace elements could be associated with the dysregulation that occurs in AMD have been reported in the literature [7,8]. In 1999, the Age-Related Eye Disease Study (AREDS) supported the idea that the supplementation of zinc (and copper to prevent hypocupremia) could help decrease the risk of the onset of AMD [7,8]. These propositions build on a wealth of literature that describes the close relationship of essential metals such as zinc and copper on ocular physiology, namely, their involvement as co-factors for superoxide dismutase and the regulation of oxidative stress. In 1995, Newsome et al. recorded zinc deficiency in those suffering from AMD, reporting a 9% decrease in zinc, and a 45% decrease in soluble zinc in aged eyes; however, they observed a significant increase in the activity of superoxide dismutase [9]. Additionally, Wong et al. reported an enhanced PRR-mediated inflammatory response caused by a zinc deficiency in aged mice [10]. Inductively coupled plasma mass spectrometry (ICP-MS) studies have been able to confirm the results found in the AREDS trials [11], noting the changes that occur in zinc and copper in the diseased and aged eye. In addition, studies into other essential elements have shown the changes to the metallome (Cd, Co, Cu, Fe, Mn, Se, and Zn) that can occur in ocular disease [12].

Essential elements such as chlorine, sulfur, and phosphorus have seldom been analysed in ICP-MS studies due to polyatomic interferences that occur with endogenous elements in an argon-based ICP-MS plasma [13]. Chlorine, however, has been implicated in AMD, with Chuang et al. showing mice with chloride intracellular channel 4 (CLIC4) deficient RPE cells ($RPE^{\Delta Clic4}$) exhibiting all the hallmarks of dry AMD, linking the CLIC4 deficiency to dysregulation of lipid metabolism and, ultimately, drusenogenesis [14]. These findings are indicative of the importance of the wider metallome and the constrictions that individual methodologies can impart to metallomic studies.

ICP-MS can offer detection limits at around 10 pg mL^{-1}, increasing to around 1 ppt for modern laser ablation (LA)-ICP-MS. This means at a spot size of 10 µm, LA-ICP-MS can be used for the production of MS images of elements in quantities less than 1 ppm in concentration [15,16]. ICP-MS is, however, subject to many factors that affect performance, such as polyatomic interferences, and elemental fractionation. Furthermore, when coupled to LA, it can suffer heavily from matrix effects, whereby more volatile material form aerosols more readily and is disproportionately represented in the ion images formed. Despite this, the past two decades have produced a wealth of data relating to the relative concentrations and distributions of metals within ocular tissue [7,11,17–19].

The MeV ion beam analysis (IBA) technique particle-induced X-ray emission (PIXE) is subject to much less interference and is not hindered by matrix effects in biological samples [20]. This allows not only for the analysis of previously complicated elements such as sulfur, phosphorus, and chlorine. Additionally, X-ray spectra are collected together with backscattered particle spectra, which is used to determine the sample matrix composition. Although the "total IBA" approach quantitative analysis can be conducted without the need for complex analytical standards as in LA-ICP-MS [21]. Consequently, the inherent problems faced by more one-dimensional studies can be overcome through the combination of complementary techniques within a multimodal workflow.

The ocular metallome has clear points of interest for the development of the understanding of ocular pathology. Information gained from wildtype (WT) mouse tissue can help to describe the ocular metallome in detail and inform on decisions in future research. In ocular research, rhodopsin knockout ($Rho^{-/-}$) tissue has long been used as a model of retinitis pigmentosa (RP), offering an insight into the structural and physiological changes that can occur as part of retinal degeneration, with homozygous mice exhibiting a complete lack of rod outer segments (OS), leading to subsequent degradation of cones and the prevention of the phototransduction cascade [22]. When studied alongside WT tissue, the structural changes that occur in a $Rho^{-/-}$ tissue could be indicative of the wider ocular metallome and how these changes may occur in retinal degeneration. Likewise, changes

within $Rho^{-/-}$ tissue can inform on the viability of the $Rho^{-/-}$ tissue in future studies of the ocular metallome.

In this study, the changes that occur within the $Rho^{-/-}$ mouse model have been nvestigated using a quantitative LA-ICP-MSI and PIXE.

2. Materials and Methods

2.1. Chemicals

The following materials were used: traceCERT® Multielement Standard Solution 6 for ICP (Merck Group, Darmstadt, Germany) HNO_3 (CAS 7697-37-2) (VWR, Poole, UK), Gelatin (Merck Group, Darmstadt, Germany), and Masson's trichrome (methyl blue) stain kit (Atom Scientific, Hyde, UK) carboxymethylcellulose (CAS 9004-32-4) (Merck Group, Darmstadt, Germany).

2.2. Tissue Collection

WT and $Rho^{-/-}$ mouse ocular tissue were obtained from Trinity College Dublin, Ireland. Ocular tissues were embedded in carboxymethylcellulose (CMC) prior to snap freezing. Sections of the ocular tissues were taken at 5 μm.

2.3. Masson's Trichrome Staining

Serial sections of both the WT and $Rho^{-/-}$ sections analysed by LA-ICP-MSI were stained using a Masson's trichrome (methyl blue) stain kit (Atom Scientific, Hyde, UK) by staining the sections in Weigart's haematoxylin for 20 min, followed by differentiation in 1% acid alcohol (99:1 EtOH:HCl). Following rinsing and blueing in water, a further stain with ponceau fuchsin was conducted for 5 min prior to rinsing and the differentiation step in water and phosphomolybdic acid for 15 min; a final stain was conducted in methyl blue for 5 min, as per the manufacturer's instructions.

2.4. Preparation of Calibration Arrays

Matrix-matched calibrants for use with LA-ICP-MSI were prepared by serial dilution with 1% HNO_3 of ICP Standard Solution 6 (Merck Group Darmstadt, Germany) to obtain 1–50 ppm solutions. These solutions were mixed 50:50 with 20% gelatin before 15 μL of each were prepared in wells created by fixing 4 mm washers in an epoxy resin. The standards were then allowed to dry in a vacuum desiccator overnight at room temperature.

2.5. LA-ICP-MS

LA-ICP-MS experiments were conducted using an ImageBio266 laser ablation unit coupled to a NexION 350X ICP-MS. The laser spot size was set to 10 μm, and the repetition rate of the laser was set to 500 Hz. The laser power was operated at 37%, resulting in a sample fluence of ~3.8 Jcm^{-1}. The ICP-MS was operated in standard mode, utilizing 5 sweeps and a dwell time of 10, 20, and 20 ms for ^{24}Mg, ^{63}Cu, and ^{66}Zn.

2.6. PIXE

WT and $Rho^{-/-}$ tissue were analysed at the National Ion Beam Centre at the University of Surrey. A 2.5 MeV (nominal beam energy) H+ beam at normal incidence was focused to a diameter <2 μm using a magnetic quadrupole triplet lens type OM-150 (Oxford Microbeams Ltd., Oxford, UK). X-rays induced by the beam were detected by a silicon drifted detector (SDD) with an active area of 80 mm^2 and mounted at a central angle of 135° to the beam direction in the horizontal plane with a variable sample-to-detector distance of 425 mm. The X-ray detector was fitted with a 130 μm beryllium foil. Elastically backscattered protons were detected using a 150 mm^2 ULTRA-series passivated implanted planar silicon (PIPS) detector (ORTEC, Wokingham, UK). The detector angle was 155° ± 0.2, and the distance between the centre of the nanobeam chamber and the detector entrance was 52.5 ± 0.2 mm. Both detectors were fitted with a sampling cone to stop signals from the chamber from reaching the detectors.

3. Results

The retinal structure is a highly privileged and highly conserved part of the ocular anatomy. Any disruption to this otherwise balanced and organized structure can cause issues for those who experience it. Elements within ocular tissue have been observed to localize discreetly within the retinal structure, conforming to the existing anatomy. The observation of elements within the retina, or the changes that occur to the elements within the ocular tissue can be descriptive of important pathophysiological mechanisms within the eye.

3.1. WT and Rho$^{-/-}$ Retinal Anatomy

Healthy mouse ocular tissue is highly structured and can be segmented into distinct layers. Figure 1 shows the choriocapillaris/RPE (CC/RPE) layer, the outer segment (OS) and inner segment (IS); the outer layers, the outer nuclear layer (ONL) and outer plexiform layer (OPL); and the inner layers, the inner nuclear layer (INL) and inner plexiform layer (IPL). The choriocapillaris is responsible for the transport of nutrients from the blood to the eye, and the other layers are key to visual function. Rods and cones function by transforming light into electrical signals, allowing the brain to transform these signals into vision. In ocular diseases such as AMD, these rods and cones are degraded by invading neovasculature in wet AMD and harmful buildups of extracellular matter known as drusen in dry AMD. The ONL and OPL, which contain the rods and cones responsible for vision, can be seen distinctly in Figure 1b. *Rho*$^{-/-}$ tissue can be seen in Figure 1. The *Rho*$^{-/-}$ tissue can be seen to have degraded this layer of the ocular tissue, leaving only the INL and the IPL intact. These structural changes that occur within the layers of the retina are severe but represent the degradation that occurs within the ocular tissue of those who have ocular degenerative diseases such as AMD, diabetic retinopathy, retinal pigmentosa, and other similar diseases.

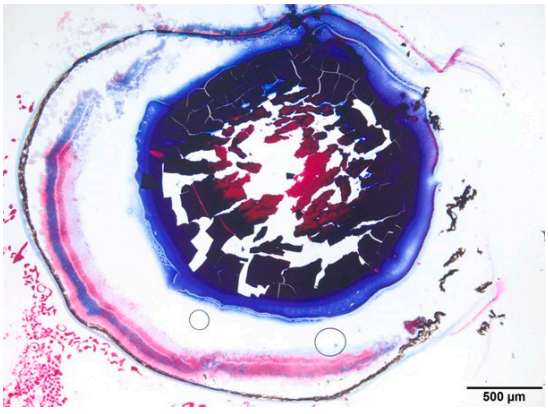

(**a**)

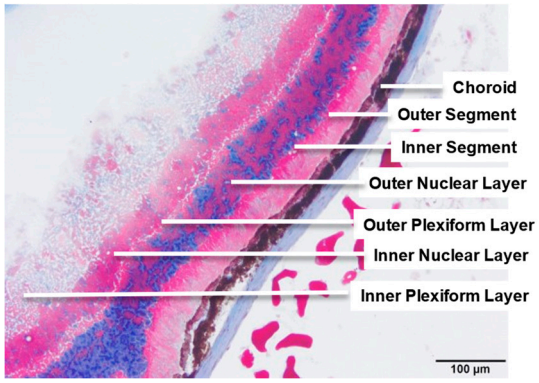

(**b**)

Figure 1. *Cont.*

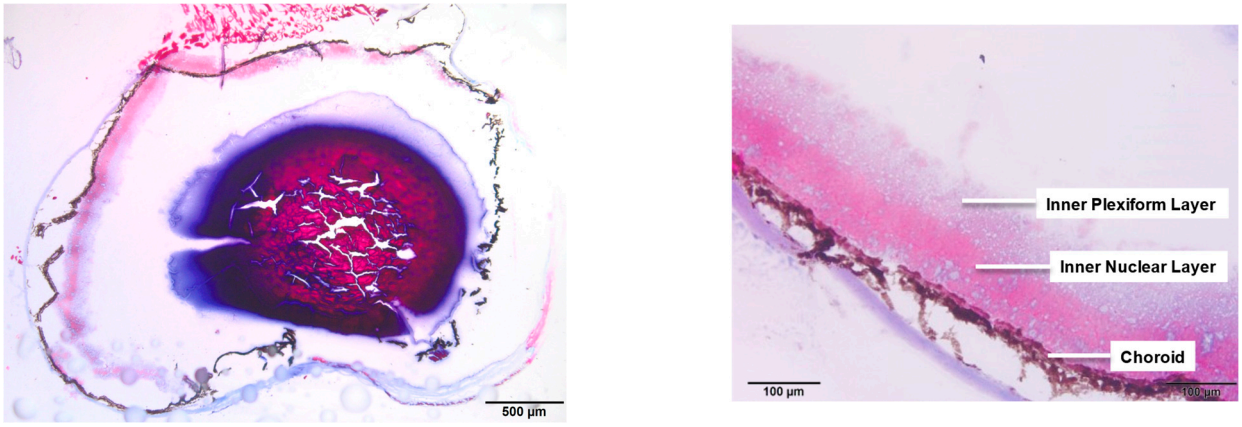

(**c**) (**d**)

Figure 1. Masson's trichrome (methyl blue) stains of wildtype mouse ocular tissue; (**a**) 20× view of the whole ocular tissue section and (**b**) 4× view of the retinal microanatomy. *Rho*$^{-/-}$ mouse ocular tissue; (**c**) 20× view of the whole ocular tissue section and (**d**) 4× view of the degraded retinal microanatomy.

3.2. LA-ICP-MSI

3.2.1. Wildtype Cu

^{63}Cu is one of the key trace metals that constitute a class of essential trace elements for ocular function. Paired with zinc, copper can be critical for the clearance of ROS in ocular tissue [10,23]. Utilizing a previously described method for the quantification of biological tissue by LA-ICP-MS [19]. WT and *Rho*$^{-/-}$ tissue were analysed alongside the calibration standards at a spot size of 10 µm to obtain high-resolution spatial characterizations of ^{63}Cu within mouse ocular tissue. Figure 2 shows the distribution of copper throughout the ocular tissue. The copper observed was largely present within all anatomical regions of the tissue, with the exception of the vitreous humor. The relative concentration, however, appeared heterogenous, with copper localizing specifically to a number of substructures of the eye, being in the highest quantity within the ciliary bodies, followed by the iris, retina, lens, and cornea, respectively. Within the retinal region, copper was observed to be most prominent in the choroid/RPE region and formed distinct bands within the retinal layers, allowing the segmentation of the retina into at least six layers of varying width. Quantitative data was produced using 250 µm wide regions of interest (ROI) placed within the substructures of the ocular anatomy by using Masson's trichrome stains of the tissue to ascertain the substructures of the microanatomy. The ROI analysis, produced in Iolite 4, allowed for the quantification of an element within a region [24–26]. Quantitative analysis showed that the concentrations ranged from just over 0.5 ppm down to just above 0.01 ppm. It also showed that the copper was in its highest quantities in the choriocapillaris, followed by the OPL, IS, INL, IPL, and OS, respectively (Figure 2).

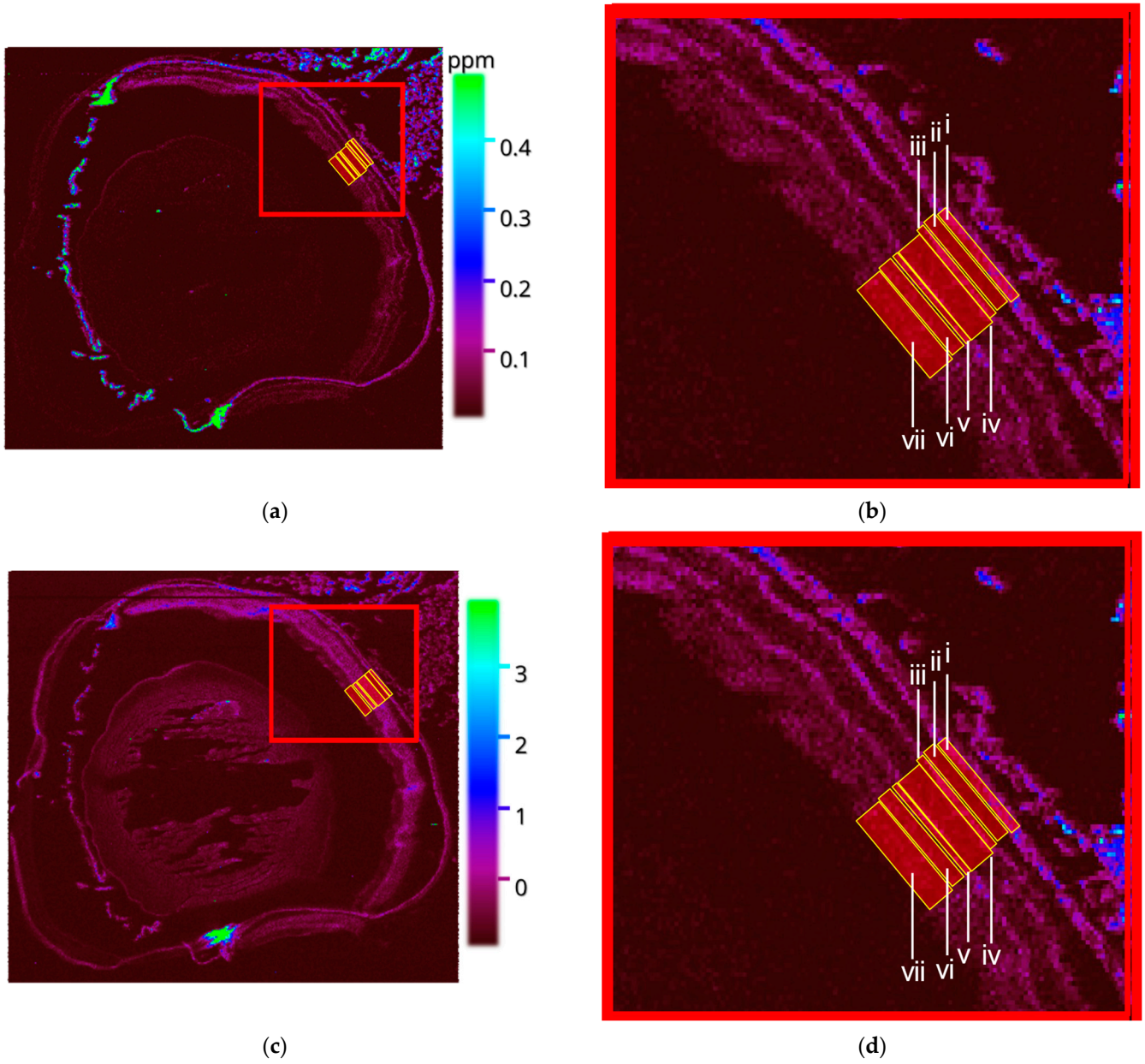

Figure 2. (**a**) Distribution of ^{63}Cu in WT mouse ocular tissue, with each region of interest (ROI) within the retinal layers highlighted (red). (**b**) A zoomed view with the portions (i) choriocapillaris (CC), (ii) outer segments (OS), (iii) inner segments (IS), (iv) outer nuclear layer (ONL), (v) outer plexiform layer (OPL), (vi) inner nuclear layers (INL), and (vii) inner plexiform layer (IPL). (**c**) Distribution of ^{66}Zn in WT mouse ocular tissue, with each region of interest (ROI) within the retinal layers highlighted (red). (**d**) A zoomed view with the portions (i) CC, (ii) OS, (iii) IS, (iv) ONL, (v) OPL, (vi) INL, and (vii) IPL.

3.2.2. Wildtype ^{66}Zn

^{66}Zn is another key element in the prevention of chronic inflammation through the upregulation of superoxide dismutase. Additionally, as previously mentioned, Zn has been observed to change as a function of age and is closely linked to AMD with AREDS 2 supplements containing a daily dose of 80 mg. Like copper, ^{66}Zn was observed within wildtype ocular tissue at a spatial resolution of 10 µm, allowing for the resolution of multiple layers within the ocular tissue. Like copper, ^{66}Zn was seen to be present within the majority of the substructures of the ocular anatomy. Unlike copper, there was less heterogeneity observed within the structures in terms of concentration. Only four distinct

regions within the retina were able to be observed, but by using the coordinates for each layer found in the copper and Masson's trichrome imaging, the same ROI analysis took place for ^{66}Zn within the retinal tissue. The quantitative analysis showed a range of 0–3 ppm, which is up to 3-fold higher than that observed for copper. ROI analysis showed that the INL, OPL, and ONL were highest in concentration followed by CC, IS IPL, and OS.

The INL, OPL, and ONL were observed to be indistinguishable but otherwise had similar relative concentrations between layers as in the Cu images.

These observed concentration changes between the CC and the rest of the tissue architecture are in agreement with previous studies of this kind, as Erie et al. described an elevated level of both copper and zinc within the CC/RPE when compared to the 'retina' in a study from 2009, which was concurrent with a 2008 study by Wills et al. [23,27].

3.2.3. Rho$^{-/-}$ Cu

Using the same quantitative and data analysis techniques as with the wildtype tissue, *Rho*$^{-/-}$ tissue was analysed by LA-ICP for both ^{66}Cu and ^{66}Zn. The copper images, like those observed in the characterization of *Rho*$^{-/-}$ tissue in Figure 1, show depletion of the OS and a complete lack of rod outer segments (OS), leading to subsequent degradation of cones, leaving only the INL and the IPL intact. The ^{63}Cu images show that other than in the retina, the distribution of copper has remained unchanged, with varying amounts of copper throughout the ocular tissue, with additional quantities in the iris and ciliary body. The retinal substructures can only be segmented into three substructures: the CC, an inner layer (INL), and an outer layer (IPL) (Figure 3). By segmenting the *Rho*$^{-/-}$ retina into three substructures, the copper and zinc observed were seen to be quite variable between replicates (Figure 4c,d), but they were generally seen to have high levels of ^{66}Zn in the CC and lower levels in the inner layers, with this difference been less pronounced in ^{63}Cu. This difference in relative concentrations between the CC and the other layers within the retina is consistent with that observed in the WT tissue. Additionally, there are few notable changes to the concentration of the ^{63}Cu and ^{66}Zn in the *Rho*$^{-/-}$ tissue. It has previously been reported that forms of ocular degeneration, and the aged retina, can lead to an elevated level of zinc and copper in aged tissue; likewise, a reduction of these elements has been observed in the AMD tissue. The results herein show how degeneration of the outer segments as part of a *Rho*$^{-/-}$ tissue type does not inherently affect the concentrations of zinc and copper within the retinal substructures that remain.

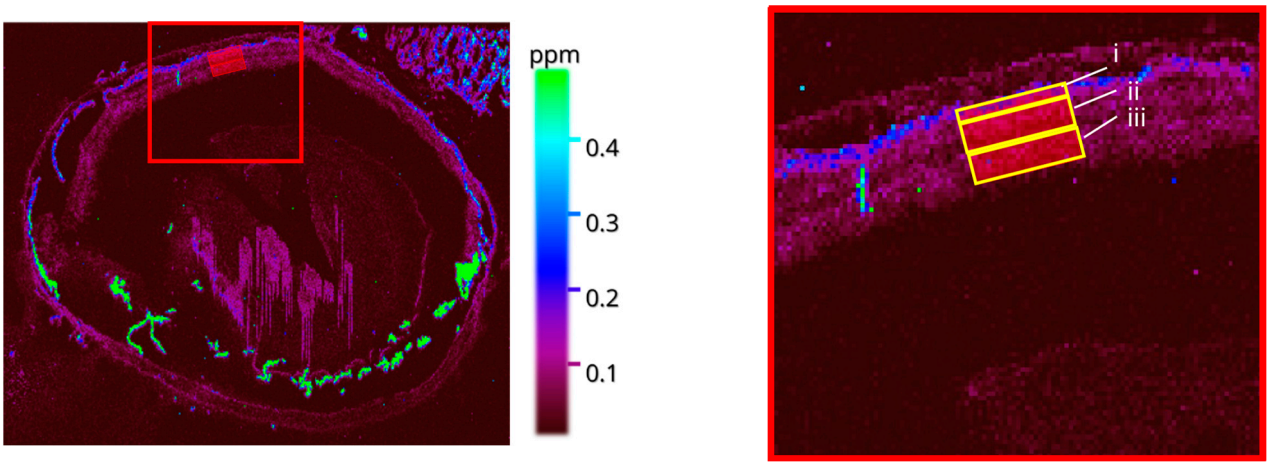

(**a**) (**b**)

Figure 3. *Cont.*

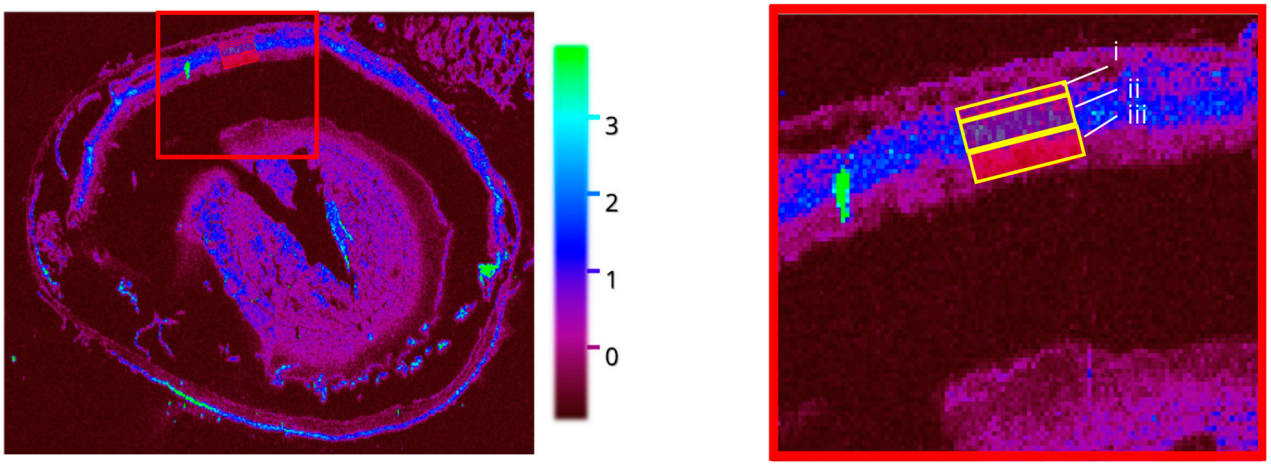

(**c**) (**d**)

Figure 3. (**a**) Distribution of ^{63}Cu in *Rho*$^{-/-}$ mouse ocular tissue, with each region of interest (ROI) within the retinal layers highlighted (red). (**b**) A zoomed view with the portions (i) choriocapillaris (CC), (ii) inner nuclear layer (INL), (iii) inner plexiform layer (IPL), (**c**) Distribution of ^{66}Zn in *Rho*$^{-/-}$ mouse ocular tissue, with each region of interest (ROI) within the retinal layers highlighted (red). (**d**) A zoomed view with the portions (i) CC, (ii) INL, and (iii) IPL.

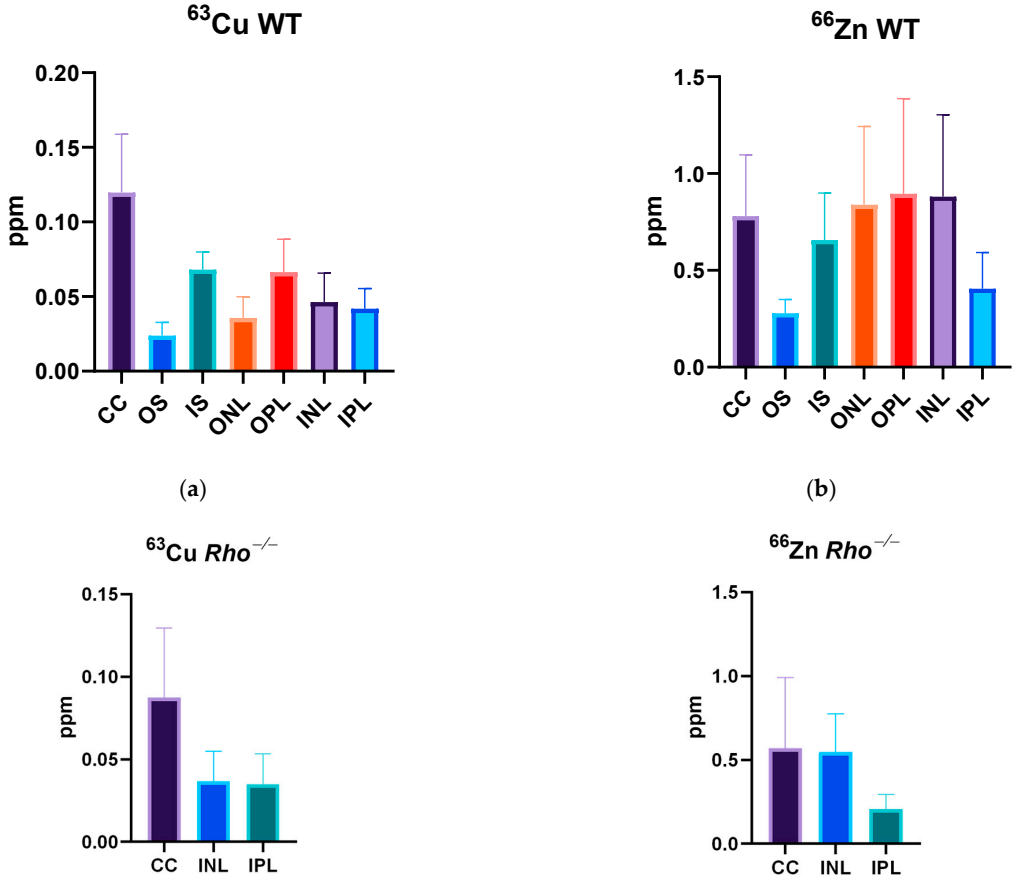

(**a**) (**b**)

(**c**) (**d**)

Figure 4. (**a**) Concentration values (ppm) of copper within a WT ocular tissue. (**b**) Concentration values (ppm) of Zn in a WT ocular tissue. (**c**) Concentration values (ppm) of copper within a *Rho*$^{-/-}$ ocular tissue. (**d**) Concentration values (ppm) of Zn in a *Rho*$^{-/-}$ ocular tissue.

3.3. PIXE

3.3.1. Phosphorus

Elements such as phosphorus (^{31}P) have interferences when analysed by an argon plasma in ICP-MS such as $^{14}N^{16}O^{1}H^{+}$, $^{15}N^{15}N^{1}H^{+}$, $^{15}N^{16}O^{+}$, $^{14}N^{17}O^{+}$, $^{13}C^{18}O^{+}$, and $^{12}C^{18}O^{1}H^{+}$ at 31 atomic mass units (amu) [13]. This means that phosphorous is virtually incompatible with argon plasma sources, as an ICP will allow the production of these nitrogen and oxygen-containing interferences from the atmosphere. Unlike ICP-MS, IBA techniques, namely, PIXE, rely on the production of characteristic X-rays, with few interferences for the PKα line. Figure 5 shows 1 mm^2 images produced from the ocular retina of mice by PIXE. Figure 5a shows how phosphorus is distributed within this ocular tissue. Like with the LA-ICP images, a clear demarcation between the retinal layers can be made; utilizing an H^+ beam focused to < 2 µm, the spatial resolution achieved was superior to that of LA-ICP-MS.

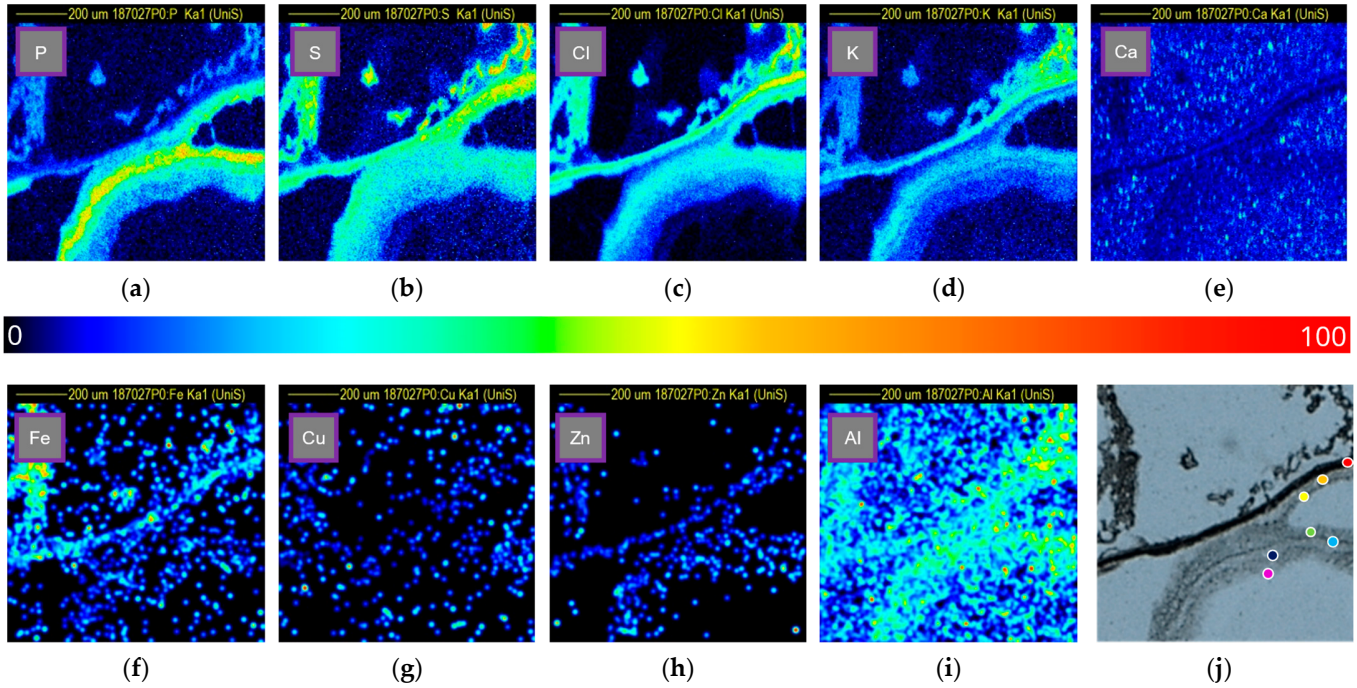

Figure 5. PIXE data detailing the retinal microanatomy of WT tissue: (**a**) phosphorous, (**b**) sulfur, (**c**) chlorine, (**d**) potassium, (**e**) calcium, (**f**) iron, (**g**) copper, (**h**) zinc, and (**i**) aluminum. (**j**) Optical image with the choroid (red), outer segment (orange), inner segment (yellow), outer nuclear layer (green), outer plexiform layer (blue), inner nuclear layer (indigo), and inner plexiform layer (violet).

In wildtype tissue, the phosphorus can be seen to localize distinctly in retinal substructures, with the highest quantities in the ONL, followed by the OPL, OS, and then the inner retinal layers (IPL and INL), which share similar concentrations to the CC.

Elevated phosphorus in the OS can be attributed to phosphatidyl-pyridinium bisretinoid (A2PE), a precursor for A2E, which is formed in the OS [28]. However, the majority of phosphorous observed can be attributed to the nuclei in the ONL, where they are associated with the high density of nucleic acids, something previously observed in ocular tissue [7].

The *Rho*$^{-/-}$ tissue was again able to demonstrate differences in tissue architecture when observed using PIXE analysis. The *Rho*$^{-/-}$ tissue showed a similarly high level of phosphorus in the INL, followed by the CC and the IPL (Figure 6a). The images show, despite the lack of observable OPL and ONL regions, that the relative concentrations of the remaining layers are consistent.

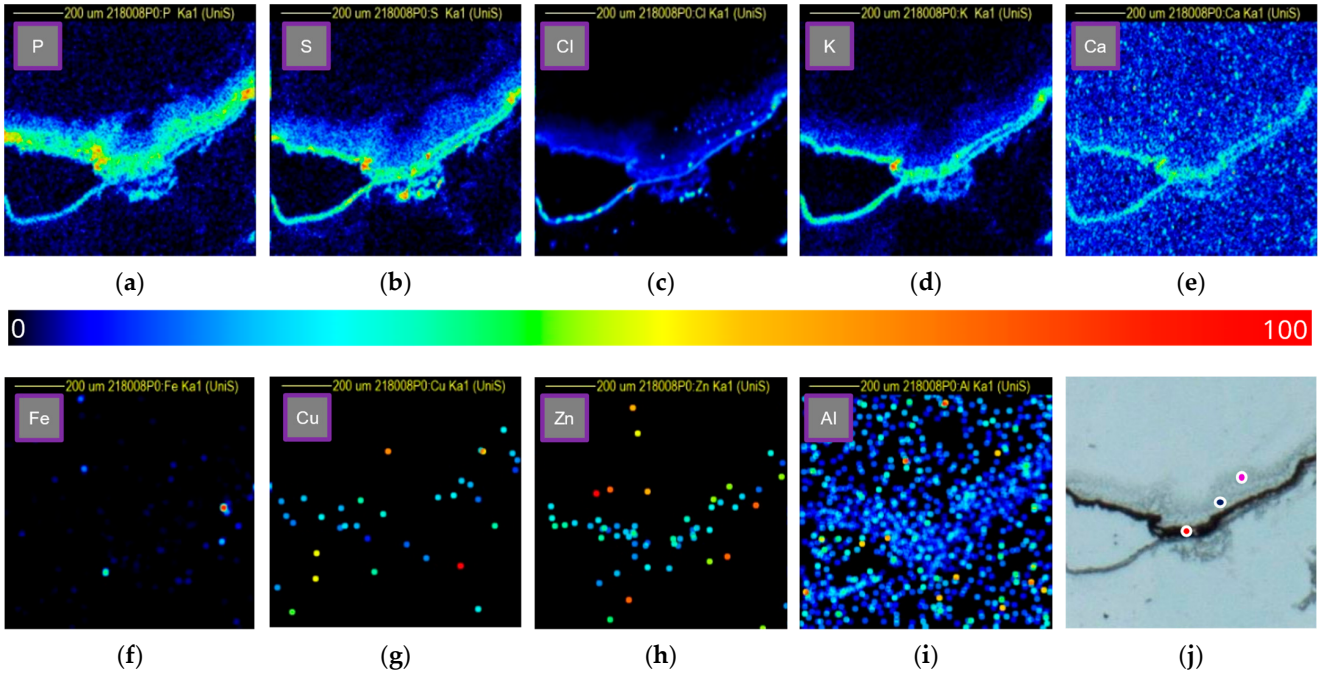

Figure 6. PIXE data detailing the retinal microanatomy of *Rho*$^{-/-}$ tissue: (**a**) phosphorous, (**b**) sulfur, (**c**) chlorine, (**d**) potassium, (**e**) calcium, (**f**) iron, (**g**) copper, (**h**) zinc, and (**i**) aluminum. (**j**) Optical image with the choroid (red), inner nuclear layer (indigo), and inner plexiform layer (violet).

3.3.2. Sulfur

Sulfur, like phosphorus, can be closely associated with the presence of proteins in structures with sulfide bonds. Sulfur is subject to polyatomic interferences when analysed by ICP with an argon plasma. Interferences from nitrogen and oxygen ($^{15}N^{18}O^{+}$, $^{14}N^{18}O^{1}H^{+}$) can cause increased levels of background noise. PIXE data (Figure 5b) exhibits the relatively homogenous distribution of sulfur within the tissue, with an increased level of sulfur in the CC and a gradual decrease in abundance moving through the OS, IS, ONL, OPL, INL, and IPL. Due to its relatively high abundance, and homogeneity, it offers a basis to determine when the beam is on or off the tissue in further PIXE analysis.

Sulfur within the *Rho*$^{-/-}$ is also able to exhibit organizational changes within the tissue. The image (Figure 6b) shows elevated sulfur in the CC, followed by a diffuse structure marking the presence of the IPL and INL. This homogeneity is observed within the IPL and INL of the WT tissue, which, like *Rho*$^{-/-}$, has the highest amount of sulfur within the CC.

3.3.3. Chlorine

Chlorine, like phosphorus, is an essential element found abundantly in the natural world and, like phosphorus, encounters issues with polyatomic interferences from the atmosphere when analysed by an argon plasma. The ^{35}Cl isotope (~76%) possesses the same mass as $^{16}O^{18}O^{1}H^{+}$, and the ^{37}Cl isotope (~24%) possesses the same mass as $^{36}Ar^{1}H^{+}$, resulting in problematic analysis when using an argon plasma ICP-MS for analysis [13]. However, chlorine has an important role in human anatomy and specifically in the retinal cycle. Chlorine is present in Ca-activated chloride channels. Chloride channels are vital for ocular function, with some involved in the control of transmitter release in the dark. Additionally, chloride intracellular channel 4 (CLIC4) is a cytosolic protein involved in the innate immune response that regulates chlorine concentration. Previously, RPE$^{\Delta Clic4}$ mice have been shown to exhibit functional and pathological hallmarks of AMD, highlighting the perceived importance of monitoring chlorine levels within the structure of the eye.

The Cl observed within WT tissue (Figure 5c) can clearly be separated into a CC, with the highest concentration, the OS, with a lower concentration the outer layers, and the inner layers of the ocular tissue, which have higher and lower concentrations, respectively, but

lower concentrations than the CC overall. The $Rho^{-/-}$ tissues once again exhibit structural changes through the lack of OSs and the depletion of the outer layers, leaving the less abundantly populated inner layers, in addition to a relatively high concentration of CC (Figure 6c).

3.3.4. Potassium

Potassium is a common essential element found within most extracellular matrices and plays a key role in the phototransduction pathways responsible for vision [29,30]. Potassium, with isotopes at 39 (93.08%), 40 (0.01%), and 41 (6.91%), has some of the most problematic interferences in $^{38}Ar^{1}H^{+}$, $^{40}Ar^{+}$, and $^{40}Ar^{1}H^{+}$, respectively [13]. This makes analysis by ICP with argon plasma extremely problematic. By using PIXE, potassium data from both WT and $Rho^{-/-}$ tissue can be ascertained. The PIXE data (Figure 5d) show potassium to be most prevalent in the CC, ONL, and INL. This, except for the more notable absence in the OPL, is a similar distribution to that of chlorine. As potassium has increased concentrations intracellularly, these results are concurrent with potassium being highly concentrated in the areas that have the highest cellular density. For potassium, once again, only the inner layers and the CC are directly observable within $Rho^{-/-}$ tissue, with little change in the distribution of potassium (Figure 6d). What remains is that the CC and the inner layers appear to have quite a high contrast in concentration in comparison to the WT data.

3.3.5. Calcium

Calcium is an essential trace element closely linked with some of the other elements aforementioned [29,30]. It has a key role within the visual cycle through modulation of the cGMP-gated channels and cGMP itself [31]. Calcium has been associated with ocular diseases such as age-related macular degeneration for some time, though its role is less clear. As part of AREDS, the National Institute for Health (NIH) showed that calcium supplementation could reduce the risk of the onset of AMD [32]. Likewise, reports of elevated levels of calcium in drusen deposits have been reported in AMD patients [33]. The distribution of calcium (Figures 5e and 6e) within ocular tissue is less distinguishable due to seemingly low levels of calcium above the background. This is because the background levels can be attributed to interferences from the PET slide on which the tissue is mounted. In spite of this, elevated levels of calcium could be observed within the CC of the WT and $Rho^{-/-}$ sections. This area within the CC, where Brusch's membrane (BrM) has its interface with the RPE, is incidentally where the calcium-filled deposits of drusen arise.

3.3.6. Iron

Iron, another element that is impaired by polyatomic interferences within an argon plasma, namely, with $^{40}Ar^{16}O^{+}$ ($=^{56}Fe$), is also of interest in ocular disease [13]. It acts as a cofactor in processes such as oxygen transport, membrane biogenesis, and maintenance of the visual cycle; more specifically, iron is essential for RPE65 activity. Iron is also heavily involved with certain mechanisms of inflammation; the Fenton reaction ($Fe^{2+} + H_2O_2 \rightarrow Fe^{3+} + HO\cdot + OH^{-}$), for example, produces ROS, which can occur as a by-product of exogenous iron accumulation, which is a phenomenon that can cause retinal degeneration [12,34,35]. These data indicate that seemingly low levels of iron can be observed predominantly in vasculature outside of the retinal anatomy, likely as part of hemoglobin, and when observed within the anatomy can be seen to be discretely localized to the CC/RPE of the ocular tissue (Figures 5f and 6f).

3.3.7. Copper

PIXE has an inferior limit of detection (ppm range) than ICP-MS, which regularly detects elements in the ppb range [16,36,37]. As a result, the copper observed in the tissue by ICP (~1.5 ppm) is at the lower end of PIXE detection limits, which were ~10 ppm across

the 1 mm^2 analysed. In Figures 5g and 6g, the images can be seen to be sparsely populated by data points as a result.

3.3.8. Zinc

Like copper, zinc remains a problematic element given that it has a <3 ppm range according to the LA-ICP-MS data (Figure 2). The data presented in the PIXE analysis were not able to obtain meaningful conclusions due to this lack of sensitivity. Unlike copper, due to its slightly higher endogenous concentration, the difference between on and off tissue was able to be determined (Figures 5h and 6h).

3.3.9. Aluminium

Similarly, aluminum had a poorer signal-to-noise ratio than previously analysed elements. The aluminum can be used to determine between on and off tissue, yet further information could not be ascertained from the images (Figures 5i and 6i).

3.4. Quantitative PIXE

PIXE analyses can be made to be quantitative without the need for matrix-matched standards. In contrast with LA-ICP-MS, this quantitative ability is compromised by matrix effects experienced in LA-ICP. The quantitative data of WT tissue showed that the endogenous elements phosphorus, sulfur, chlorine, potassium, and calcium were in significantly higher quantities than that of copper and zinc. Chlorine was seen to be in its highest concentration in the CC, where it also exceeded the concentrations of P, S, K, and Ca. Phosphorus was seen to be the highest within the ONL, followed by chlorine, sulfur, and potassium. The highest level metal in the INL was, however, sulfur by a factor of two. The third region (Figure 7b), which described the PET slide on which the slides were analysed, was, however, indicative of the interferences that can be seen in PIXE analysis. The Ca images (Figures 6e and 7e), which were relatively indiscriminate, can be explained by the high presence of Ca within the PET film as seen in Figure 7. The quantitative data show that Ca is not homogenously distributed, yet the signal-to-noise ratio remains too low for discerning structural features. Iron, copper, zinc, and aluminum were in low abundance and were thereby unable to be quantified accurately (Figure S1).

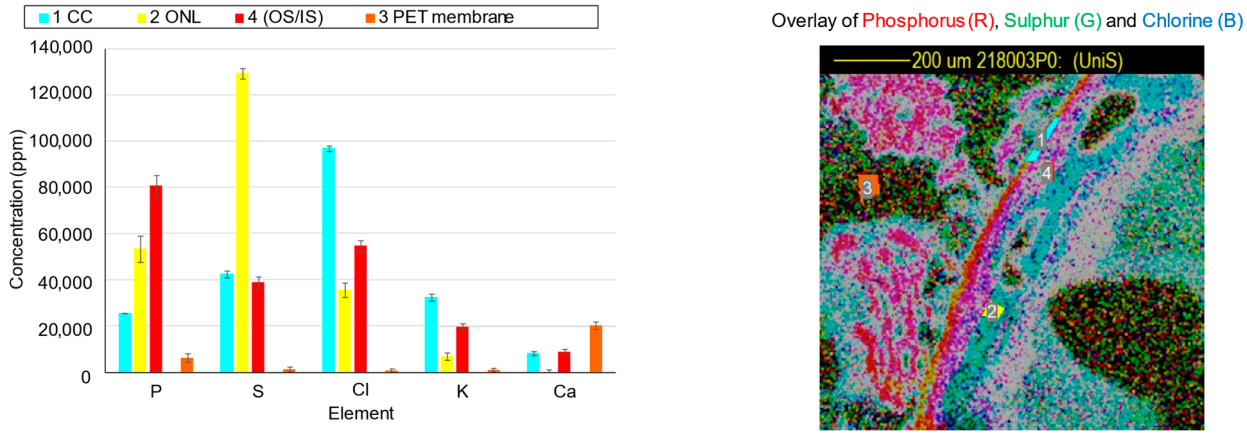

(**a**) (**b**)

Figure 7. Quantitative PIXE data exhibiting the concentrations of the elements phosphorus, sulfur, chlorine, potassium, and calcium. (**a**) Concentrations (ppm) of the regions of interest (ROI) within a wildtype (WT) tissue. (**b**) An image of the corresponding WT tissue section ROIs; (1) choriocapillaris (CC) (2) outer nuclear layer (ONL) (3) polyethylene terephthalate (PET) (4) outer/inner segment (OS/IS).

4. Discussion and Conclusions

The use of LA-ICP-MS in the exploration of ocular pathology has been able to offer unique insights into the metallome of WT ocular tissue in the past, though it has been at the mercy of matrix effects and polyatomic interferences that LA-ICP-MS is notoriously susceptible to. This body of work comprises a combination of quantitative LA-ICP-MSI and PIXE analysis and has comprehensively described the metallome of not only elements amenable to ICP-MS analysis such as copper and zinc, but also to the wider metallome excluded by studies confined to ICP-MS analysis such as phosphorus, sulfur, chlorine, potassium, calcium, and iron. Additionally, the datasets herein include a widely used retinal degeneration model, $Rho^{-/-}$, which has described the structural changes that occur within $Rho^{-/-}$ tissue from the perspective of the metallome. This study has demonstrated the changes that occur to the metal species within $Rho^{-/-}$ tissue and how the changes to the structure affect the distribution of essential elements. With a wider understanding of not only the WT metallome but that of $Rho^{-/-}$ tissue as well, this study contributes to the wider understanding of ocular tissue and how elements from across the periodic table behave in the retina.

From the essential elements measured within WT ocular tissue, it can be seen that there is a highly organized structure within the mouse retina [38]. The distributions of these elements, however, are not uniform to one another, some elements remain relatively homogenous through different layers within the retina, whereas copper can be seen to vary in concentration distinctly between each identifiable layer within the retina. The existence of this complex relationship between structure function and the wider metallome is poorly understood; however, the high spatial resolution imaging of these structures may help to inform ocular physiology and pathology in the future. In addition, the ocular tissue from the $Rho^{-/-}$ mice demonstrated the structural changes that have occurred as a result of the deletion of rhodopsin. The retinal tissue of $Rho^{-/-}$ mice has reduced structural organization and is missing layers, namely, the outer segments. In LA-ICP-MS and PIXE images, these structural changes can be seen to occur but do not affect the distribution or relative concentrations of the metals observed. These data, however, were purely qualitative; so, should further quantitative work be undertaken in the future, some physiological as well as structural changes may be observed through mapping elemental concentrations in $Rho^{-/-}$ tissue.

The metallome is a widely explored yet poorly understood part of ocular pathology, yet methodologies and techniques for the characterization of such tissue have become increasingly more accessible in recent years. In addition, the use of multimodal workflows has greatly benefitted the field of metallomics, with PIXE and LA-ICP-MS as prime examples of complimentary datasets, utilizing the sensitivity of ICP and the robustness and spatial resolution of PIXE. These data demonstrate a foundation by which future studies relating to the ocular metallome may build, utilizing more complex sample sets and eventually progressing to patient tissue.

Supplementary Materials: The following supporting information can be downloaded at: https://www.mdpi.com/article/10.3390/analytica4030021/s1, Figure S1 PIXE Spectrum showing insufficient sensitivity for quantification of Al, Fe, Cu, and Zn.

Author Contributions: Conceptualization, L.M.C., S.D., C.D., C.C., M.J.B. and J.M.; methodology, J.M., L.G., C.C., J.v.G. and E.S.; validation, J.M., E.S., C.C., J.v.G. and M.J.B.; formal analysis, J.M., C.C., J.v.G. and E.S.; investigation, J.M., C.C., J.v.G. and E.S.; resources, S.D., L.G., C.C., M.J.B., E.S. and J.v.G.; data curation, J.M., C.C., J.v.G. and E.S.; writing—original draft preparation, J.M.; writing—review and editing, L.M.C. and M.J.B.; supervision, L.M.C., C.D., S.D. and S.C.; project administration, L.M.C.; funding acquisition, L.M.C., J.M. and S.D. All authors have read and agreed to the published version of the manuscript.

Funding: This project has received funding from the European Union's Horizon 2020 research and innovation programme under grant agreement No 824096 and the UK National Ion Beam Centre Pump Priming Scheme under EP/X015491/1 and EP/R031118/1.

Data Availability Statement: The data presented in this study will be made available at the Sheffield Hallam University Research Data Archive SHURDA and will be able to be found at https://shurda.shu.ac.uk, accessed on 28 June 2023.

Acknowledgments: We thank Rob Hutchinson (Elemental Scientific Lasers) for his expertise in working with novel equipment. For the purpose of open access, the author has applied a Creative Commons Attribution (CC BY) license to any author accepted manuscript version arising from this submission.

Conflicts of Interest: The authors declare no conflict of interest.

Abbreviations

AMD	Age-Related Macular Degeneration
amu	Atomic mass unit
AREDS	Age Related Eye Disease Study
BrM	Brusch's Membrane
CC	Chorio Capillaris
CLIC4	Chliride Intracellular Channel 4
CMC	Carboxymethylcellulose
DAMPS	Damage-Associated Molecular Patterns
ESL	Elemental Scientific Lasers
IBA	Ion Beam Analysis
ICP	Inductively Coupled Plasma
INL	Inner Nuclear Layer
IPL	Inner Plexiform Layer
IS	Inner Segment
LA	Laser Ablation
MS	Mass Spectrometry
ONL	Outer Nuclear Layer
OPL	Outer Plexiform Layer
OS	Outer Segment
PET	Polyethylene Terephthalate
PIPS	Passivated Implanted Planar Silicon
PIXE	Particle-Induced X-Ray Emission
PRR	Pattern Recognition Receptors
RHO	Rhodopsin
ROI	Region Of Interest
ROS	Reactive Oxygen Species
RP	Retinis Pigmentosa
RPE	Retinal Pigment Epithelium
SDD	Silicon Drifted Detector
WT	Wildtype

References

1. Bourne, S.R.; Flaxman, H.R.; Taylor, R.J.; Casson, A.; Abdoli, E.; Abu-Gharbieh, A.A.; Alamneh, W.; Alemayehu, V.; Alipour, E.W.; Anbesu, J.; et al. Trends in prevalence of blindness and distance and near vision impairment over 30 years: An analysis for the Global Burden of Disease Study. *Lancet Glob. Health* **2021**, *9*, e130–e143. [CrossRef] [PubMed]
2. Papadopoulos, Z. Recent Developments in the Treatment of Wet Age-related Macular Degeneration. *Curr. Med. Sci.* **2020**, *40*, 851–857. [CrossRef]
3. Celkova, L.; Doyle, S.L.; Campbell, M. NLRP3 Inflammasome and Pathobiology in AMD. *J. Clin. Med.* **2015**, *4*, 172–192. [CrossRef]
4. The Age-Related Eye Disease Study Research Group. The effect of five-year zinc supplementation on serum zinc, serum cholesterol and hematocrit in persons randomly assigned to treatment group in the age-related eye disease study: AREDS Report No. 7. *J. Nutr.* **2002**, *132*, 697–702. [CrossRef] [PubMed]
5. Rock, K.L.; Latz, E.; Ontiveros, F.; Kono, H. The Sterile Inflammatory Response. *Annu. Rev. Immunol.* **2009**, *28*, 321–342. [CrossRef]
6. Guo, H.; Callaway, J.B.; Ting, J.P. Inflammasomes: Mechanism of action, role in disease and therapeutics. *Nat. Med.* **2015**, *21*, 677–687. [CrossRef]
7. Pålsgård, E.; Ugarte, M.; Rajta, I.; Grime, G. The role of zinc in the dark-adapted retina studied directly using microPIXE. *Nucl. Instruments Methods Phys. Res. Sect. B Beam Interactions Mater. Atoms* **2001**, *181*, 489–492. [CrossRef]

8. Randomized, A. Placebo-Controlled, Clinical Trial of High-Dose Supplementation With Vitamins C and E, Beta Carotene, and Zinc for Age-Related Macular Degeneration and Vision Loss: AREDS Report No. 8. *Arch. Ophthalmol.* **2001**, *119*, 1417–1436.
9. Newsome, D.A.; Miceli, M.V.; Tate, D.J.; Alcock, N.W.; Oliver, P.D. Zinc content of human retinal pigment epithelium decreases with age and macular degeneration, but superoxide dismutase activity increases. *J. Trace Elem. Exp. Med.* **1996**, *8*, 193–199. [CrossRef]
10. Wong, C.P.; Rinaldi, N.A.; Ho, E. Zinc deficiency enhanced inflammatory response by increasing immune cell activation and inducing IL6 promoter demethylation. *Mol. Nutr. Food Res.* **2015**, *59*, 991–999. [CrossRef]
11. Ugarte, M.; Osborne, N.N. Recent advances in the understanding of the role of zinc in ocular tissues. *Metallomics* **2014**, *6*, 189–200. [CrossRef] [PubMed]
12. Jünemann, A.G.; Stopa, P.; Michalke, B.; Chaudhri, A.; Reulbach, U.; Huchzermeyer, C.; Schlötzer-Schrehardt, U.; Kruse, F.E.; Zrenner, E.; Rejdak, R. Levels of Aqueous Humor Trace Elements in Patients with Non-Exsudative Age-related Macular Degeneration: A Case-control Study. *PLoS ONE* **2013**, *8*, e56734. [CrossRef]
13. May, T.W.; Wiedmeyer, R.H. A table of polyatomic interferences in ICP-MS. *At. Spectrosc.* **1998**, *19*, 150–155.
14. Chuang, J.Z.; Yang, N.; Nakajima, N.; Otsu, W.; Fu, C.; Yang, H.H.; Lee, M.P.; Akbar, A.F.; Badea, T.C.; Guo, Z.; et al. Retinal pigment epithelium-specific CLIC4 mutant is a mouse model of dry age-related macular degeneration. *Nat. Commun.* **2022**, *13*, 374. [CrossRef]
15. Trueman, C. *Encyclopedia of Analytical Science*, 2nd ed.; Worsfold, P., Townshend, A., Poole, C., Eds.; Elsevier: Oxford, UK, 2005; pp. 171–181.
16. Limbeck, A.; Galler, P.; Bonta, M.; Bauer, G.; Nischkauer, W.; Vanhaecke, F. Recent advances in quantitative LA-ICP-MS analysis: Challenges and solutions in the life sciences and environmental chemistry. *Anal. Bioanal. Chem.* **2015**, *407*, 6593–6617. [CrossRef]
17. Ugarte, M.; Osborne, N.N.; Brown, L.A.; Bishop, P.N. Iron, zinc, and copper in retinal physiology and disease. *Surv. Ophthalmol.* **2013**, *58*, 585–609. [CrossRef] [PubMed]
18. Aberami, S.; Nikhalashree, S.; Bharathselvi, M.; Biswas, J.; Sulochana, K.N.; Coral, K. Elemental concentrations in Choroid-RPE and retina of human eyes with age-related macular degeneration. *Exp. Eye Res.* **2019**, *186*, 107718. [CrossRef]
19. Millar, J.; Ozaki, E.; Campbell, S.; Duckett, C.; Doyle, S.; Cole, L.M. Multiomic Mass Spectrometry Imaging to Advance Future Pathological Understanding of Ocular Disease. *Metabolites* **2022**, *12*, 1239. [CrossRef]
20. Greenhalgh, C.J.; Karekla, E.; Miles, G.J.; Powley, I.R.; Costa, C.; De Jesus, J.; Bailey, M.J.; Pritchard, C.; MacFarlane, M.; Pringle, J.H.; et al. Exploration of Matrix Effects in Laser Ablation Inductively Coupled Plasma Mass Spectrometry Imaging of Cisplatin-Treated Tumors. *Anal. Chem.* **2020**, *92*, 9847–9855. [CrossRef]
21. Jeynes, C.; Bailey, M.J.; Bright, N.J.; Christopher, M.E.; Grime, G.W.; Jones, B.N.; Palitsin, V.V.; Webb, R.P. "Total IBA"–Where are we? *Nucl. Instrum. Methods Phys. Res. Sect. B Beam Interact. Mater. At.* **2012**, *271*, 107–118. [CrossRef]
22. Jaissle, G.B.; May, C.A.; Reinhard, J.; Kohler, K.; Fauser, S.; Lutjen–Drecoll, E.; Zrenner, E.; Seeliger, M.W. Evaluation of the Rhodopsin Knockout Mouse as a Model of Pure Cone Function. *Investig. Ophthalmol. Vis. Sci.* **2001**, *42*, 506–513.
23. Wills, N.; Ramanujam, V.S.; Kalariya, N.; Lewis, J.; van Kuijk, F. Copper and zinc distribution in the human retina: Relationship to cadmium accumulation, age, and gender. *Exp. Eye Res.* **2008**, *87*, 80–88. [CrossRef] [PubMed]
24. Petrus, J.A.; Chew, D.M.; Leybourne, M.I.; Kamber, B.S. A new approach to laser-ablation inductively-coupled-plasma mass-spectrometry (LA-ICP-MS) using the flexible map interrogation tool 'Monocle'. *Chem. Geol.* **2017**, *463*, 76–93. [CrossRef]
25. Paton, C.; Hellstrom, J.; Paul, B.; Woodhead, J.; Hergt, J. Iolite: Freeware for the visualisation and processing of mass spectrometric data. *J. Anal. At. Spectrom.* **2011**, *26*, 2508. [CrossRef]
26. Woodhead, J.D.; Hellstrom, J.; Hergt, J.M.; Greig, A.; Maas, R. Isotopic and Elemental Imaging of Geological Materials by Laser Ablation Inductively Coupled Plasma-Mass Spectrometry. *Geostand. Geoanalytical Res.* **2007**, *31*, 331–343. [CrossRef]
27. Erie, J.C.; Good, J.A.; Butz, J.A.; Pulido, J.S. Reduced Zinc and Copper in the Retinal Pigment Epithelium and Choroid in Age-related Macular Degeneration. *Am. J. Ophthalmol.* **2009**, *147*, 276–282.e1. [CrossRef]
28. Boyer, N.P.; Higbee, D.; Currin, M.B.; Blakeley, L.R.; Chen, C.; Ablonczy, Z.; Crouch, R.K.; Koutalos, Y. Lipofuscin and N-retinylidene-N-retinylethanolamine (A2E) accumulate in retinal pigment epithelium in absence of light exposure: Their origin is 11-cis-retinal. *J. Biol. Chem.* **2012**, *287*, 22276–22286. [CrossRef] [PubMed]
29. Bito, L.Z.; DiBenedetto, F.E.; Stetz, D. Homeostasis of the retinal micro-environment: I. Magnesium, potassium and calcium distributions in the avian eye. *Exp. Eye Res.* **1982**, *34*, 229–237. [CrossRef]
30. Mannu, G.S. Retinal phototransduction. *Neurosciences* **2014**, *19*, 275–280. [PubMed]
31. Nakatani, K.; Chen, C.; Yau, K.; Koutalos, Y. *Advances in Experimental Medicine and Biology*; Springer USA: Boston, MA, USA, 2002; pp. 1–20.
32. Tisdale, A.K.; Agrón, E.; Sunshine, S.B.; Clemons, T.E.; Ferris, F.L.; Chew, E.Y. Association of Dietary and Supplementary Calcium Intake With Age-Related Macular Degeneration: Age-Related Eye Disease Study Report 39. *Arch. Ophthalmol. (1960)* **2019**, *137*, 543–550. [CrossRef]
33. Flinn, J.M.; Kakalec, P.; Tappero, R.; Jones, B.; Lengyel, I. Correlations in distribution and concentration of calcium, copper and iron with zinc in isolated extracellular deposits associated with age-related macular degeneration. *Metallomics* **2014**, *6*, 1223–1228. [CrossRef]
34. Wong, R.W.; Dchimene, R.; Hahn, P.; Green, W.R.; Dunaief, J.L. Iron Toxicity as a potential factor in AMD. *Retina* **2007**, *27*, 997–1003. [CrossRef] [PubMed]

35. Hahn, P. Maculas affected by age-related macular degeneration contain increased chelatable iron in the retinal pigment epithelium and Bruch's membrane. *JAMA* **2003**, *290*, 2525. [CrossRef] [PubMed]
36. Christopher, M.E.; Warmenhoeven, J.W.; Romolo, F.S.; Donghi, M.; Webb, R.P.; Jeynes, C.; Ward, N.I.; Kirkby, K.J.; Bailey, M.J. A new quantitative method for gunshot residue analysis by ion beam analysis. *Analyst* **2013**, *138*, 4649–4655. [CrossRef] [PubMed]
37. dos Santos, C.E.I.; da Silva, L.R.M.; Boufleur, L.A.; Debastiani, R.; Stefenon, C.A.; Amaral, L.; Yoneama, M.L.; Dias, J.F. Elemental characterisation of Cabernet Sauvignon wines using Particle-Induced X-ray Emission (PIXE). *Food Chem.* **2010**, *121*, 244–250. [CrossRef]
38. Ash, J.D.; Grimm, C.; Hollyfield, J.G.; Anderson, R.E.; LaVail, M.M.; Bowes, C.R. *Retinal Degenerative Diseases*; Springer: New York, NY, USA, 2014.